



Complex interplay of structural and surface properties of ceria on platinum supported catalyst under water gas shift reaction



D.M. Meira ^{a,b}, R.U. Ribeiro ^a, O. Mathon ^b, S. Pascarelli ^b, J.M.C. Bueno ^a, D. Zanchet ^{c,*}

^a Department of Chemical Engineering, Federal University of São Carlos, C.P. 676, 13565-905, São Carlos, São Paulo, Brazil

^b European Synchrotron Radiation Facility, B.P. 220, F-38043 Grenoble Cedex, France

^c Chemistry Institute, University of Campinas, C.P. 6154, 13083-970, Campinas, São Paulo, Brazil

ARTICLE INFO

Article history:

Received 22 February 2016

Received in revised form 7 April 2016

Accepted 14 April 2016

Available online 30 April 2016

Keywords:

Platinum supported catalysts

Ceria

Water-gas shift reaction

Structural properties

ABSTRACT

Catalysts using platinum pre-formed nanoparticles were prepared as a strategy to evaluate the impact of structural and electronic properties of ceria-alumina-supports in the water gas shift reaction, minimizing variations of the metallic phase among samples. Promoted cerium Pt/Al₂O₃ catalysts, with 12 or 20 wt% of CeO₂, were prepared by adding cerium precursor during the sol-gel synthesis of Al₂O₃ (GEL samples) or by impregnating it on the Al₂O₃ support (IMP samples). The presence of cerium in PtAl catalysts increases up to seven times the reaction rates and although the results showed significant impact of the preparation method on the structural and surface properties of ceria, the main dependence of the catalytic activity seems to be with the cerium loading. The results suggest the participation of interfacial Pt—O—Ce sites as the crucial contribution to the significant increases of specific reaction rate.

© 2016 Elsevier B.V. All rights reserved.

1. Introduction

In the water gas shift (WGS) reaction, CO reacts with steam producing CO₂ and H₂. It is an important reaction to decrease the CO level in the syngas, deriving from the process of steam reforming of natural gas or other sources. In addition, WGS is one of the main reactions to produce H₂ at industrial scale. Industrially, it is performed in two steps: the first one at high temperature, with iron-based catalysts, and the second one at low temperature, with copper-based catalysts [1]. Recently, the development of PEM (proton exchange membrane) fuel cell technology, which requires H₂ with low CO levels, has boosted the search for new WGS catalysts.

Platinum is a non-pyrophoric WGS catalyst with high activity but the stability of Pt nanoparticles and their activity depends on the nature of the support [2–6]. One of the most studied supports is ceria. Thirty years ago, changes on ceria redox behavior caused by the interaction with platinum were demonstrated [7,8]. Later, several studies pointed out that Pt is anchored on CeO₂ through Pt—O—Ce bond, improving Pt stability and its catalytic properties [5,9–12].

Cerium has a low redox potential changing its oxidation state from Ce⁴⁺ to Ce³⁺ and leading to the formation of non-

stoichiometric oxides (CeO_{2-x}), with capacity to store and release oxygen dependent on the atmosphere [8]. It has been shown that several aspects such as crystallographic orientation in cerium oxide, particle size, presence of doping atoms (Ti⁴⁺, La³⁺, Zr⁴⁺, etc.), presence of alkali metals, among others, affect the formation of oxygen vacancies, the interaction with gases and/or the interaction with metallic particles impacting its catalytic performance [13–22]. Nevertheless, one important aspect that has not been deeply tackled is the direct impact of the structural characteristics of nm-sized ceria phase in the overall activity.

Despite extensive work, some issues about WGS on Pt-ceria remain under intense debate: (i) the main reaction mechanism, (ii) the reaction rate limiting step, (iii) the species that are real intermediates and those that are mere spectators and (iv) the adsorption sites (e.g., on metal, support or interface). Two main mechanisms have been discussed: redox and associative [15,23–28]. The redox pathway involves the participation of O atoms from the support while the associative mechanism the O is provided by H₂O activation. Variants such as associative with redox regeneration involving OH species generated with the O from the support have been proposed [27]. The intermediaries such as formates, carboxylates, carbonates, etc, that are formed in the associative pathway have also been debated. It seems now consensus that a unified mechanism for all Pt catalysts does not exist, depending on the Pt size, support and interaction as well as on the catalytic conditions.

* Corresponding author.

E-mail address: daniel@iqm.unicamp.br (D. Zanchet).

To address these questions, different approaches have been adopted. To evaluate the role of the metallic phase and support, for example, metal loading, particle size and composition are varied using the same support; or the metal loading is fixed and the support composition is varied. By tuning parameters such as size, shape, structure and composition of both phases, it has been possible to highlight not only the metal influence but also the support and the metal-support influence [17,20,22,23,29–33]. For example, by comparing Pt/CeO₂ with Ru/CeO₂ and Pt–Ru/CeO₂ catalysts, Xu et al. [34] showed that the vacancies formation and the CO adsorption were favored by alloying Pt with Ru while the formation of formates and methane production decreased. However, alloy formation did not affect activity indicating that formates were spectators or were not involved in the main reaction pathway in the used conditions. When Pt and CeO_x were co-deposited on TiO₂ [6,16,22], a higher degree of reduction of the CeO_x nanoparticles was observed under WGS and assigned as a key factor to explain the improved catalytic performance of this catalyst. Kalamaras et al. [17] studied Pt/Ce_xZr_{1-x}O₂ catalysts and also correlated the increase in the number of vacancies in the CeO₂ lattice due to Zr addition to the enhanced catalytic activity. The reaction pathway was extremely dependent on the reaction temperature, Ce/Zr atomic ratio and Pt particle size, the latter in accordance to the structure-sensitive nature of the WGS reaction. The correlation between catalyst activity and its reducibility was also studied on platinum ceria and ceria-gallia catalysts but different conclusions were obtained [15]. Although the data confirmed that activation of water involves oxygen vacancy filling in the support, this is a fast process and not the rate-determining step. This contrast with conclusions from earlier works by Rodriguez et al. [35] and Bruix et al. [29]. Concerning the reaction mechanism, Vecchietti et al. [15] suggested that monodentate formate and carboxylate are reaction intermediates and are located at the metal-support interface while carbonate and bidentate formate are spectators.

Important insights about the reaction mechanisms have been obtained by SSITKA (Steady-State Isotopic Transient Kinetics Analysis) coupled with spectroscopic techniques, such as DRIFTS (Difuse Reflectance Infrared Fourier Transform Spectroscopy) [25,36,37]. In the case of Pt supported on CeO₂, extensive work in a broad set of catalyst [17–23,38] clearly show a bifunctional mechanism operating in this system, in which both Pt particle size and the nature of the support directly impact on the number and kind of active sites. The main mechanism is also dependent on the catalytic conditions [23,25]. In addition, DFT (Density Functional Theory) calculations are also helping to improve the knowledge about the WGS reaction mechanism. Recent work by Clay et al. [39] suggests that even in the case of Pt supported on Al₂O₃, considered an “inert” support, the support plays an active role. In the case of Pt on CeO₂, this has been clearly demonstrated [27–29,40]. Despite the kinetic parameters and energies found by DFT are still not fully consistent with the experimental ones [27,28,39], DFT is helping to point out the most energetically favored pathways. For example, Aranifard et al. [27,28] showed the importance of associative carboxyl mechanism on Pt/CeO₂ and that a formate mechanism is energetically unfavored in the analyzed framework.

Therefore, in the case of Pt supported on CeO₂ a complex scenario takes place, and in this context, it is known that catalyst properties can be significantly affected under reaction conditions and *in situ* studies are critical to correctly access catalyst electronic and structural properties [11,12,41–47]. In addition, the use of pre-formed colloidal nanoparticles, with narrow size distribution, has provided an insightful approach to produce model catalysts, to address independently and in an uncorrelated way several parameters such as composition, size, shape and structure of either metallic or oxide phase [48–50].

In this work, we performed a detail characterization of platinum-cerium-alumina model catalysts under WGS conditions by using *in situ* techniques and pre-formed platinum nanoparticles (Pt-NPs), which were encapsulated in Al₂O₃ sol-gel modified with CeO₂ or encapsulated in CeO₂–Al₂O₃ sol-gel. Our results show a lack of direct dependence of the activity with the average ceria structural properties suggesting that the creation of the interfacial Pt–O–Ce sites is likely to be the limiting factor in these samples.

2. Experimental

2.1. Catalysts preparation

The synthesis of Pt-alumina catalyst is described elsewhere [49]. Briefly, colloidal Pt-NPs protected by polyvinilpirrolidone (PVP), with 2.8 nm diameter, were added during the sol-gel synthesis of bohemite to produced, after drying the gel and calcining at 500 °C, the PtAl catalyst (1.5 wt% Pt).

Promoted cerium PtAl catalysts, with 12 or 20 wt% of CeO₂, were prepared by two methods, both using Ce(NO₃)₃·6H₂O (99.9% Aldrich) as precursor. In the first one, an aqueous solution of cerium precursor was added to the initial solution of the sol-gel synthesis of bohemite, in the presence of the Pt-NPs [50,51]. After drying the gel, the samples were calcined at 500 °C (4 °C min⁻¹, under synthetic air for 4 h). The catalysts were labeled as g-PtxCeAl (x = 12 or 20 wt% CeO₂) and generally referred as the “GEL samples” because the Ce precursor was added during the sol-gel synthesis of the bohemite. In the second method, the PtAl catalyst was impregnated with the appropriate amount of 0.07 M of cerium precursor and a second calcination at 500 °C (4 °C min⁻¹, under synthetic air for 4 h) was performed. The catalysts were labeled i-xCePtAl (x = 12 or 20 wt% CeO₂) and generally referred as the “IMP samples” because the Ce precursor was impregnated on the PtAl catalyst.

2.2. Characterization

Specific surface area (S_{BET}) was measured by N₂ adsorption–desorption isotherms at –196 °C, using a Quanta Chrome Nova 1200. The samples were degassed at 200 °C under vacuum for 2 h. The S_{BET} was calculated using the Brunauer, Emmett and Teller (BET) method.

X-ray diffraction (XRD) patterns were collected with a Rigaku Miniflex DMAX 2500 PC (30kV–10 mA) diffractometer and Cu K α radiation ($\lambda = 1.5418 \text{ \AA}$) and 2 θ ranging from 5 to 90° with a scan rate of 2 min⁻¹ and step of 0.02°.

Fourier transformed Infrared (FTIR) spectra with CO adsorption were recorded using a Thermo Nicolet iS50 FTIR spectrophotometer equipped with MCT detector and a Harrick diffuse reflectance infrared Fourier transform spectroscopy cell with CaF₂ windows. CO adsorption measurements of supported catalysts were carried out using approximately 80 mg of sample. The samples were pre-reduced at 500 °C (10 °C min⁻¹) under a mixture of 25% H₂ in N₂ flowing at 45 mL min⁻¹ for 1 h. The samples were cooled to 25 °C in N₂ and FTIR spectra (64 scans at 4 cm⁻¹ resolution) were collected after 5 min exposure of the catalysts to CO at 25 °C and 20 Torr.

X-ray photoelectron spectroscopy (XPS) spectra were obtained with a SPECSLAB II (Phoibos-Hsa 3500 150, 9 channeltrons) SPECS spectrometer equipped with an Al K α source (1487 eV, E_{pass} = 40 eV, energy step = 0.2 eV, and acquisition time = 2 s per point) at Brazilian Synchrotron Light Laboratory (LNLS). Samples were prepared as pellets (100 mg), transferred to the XPS pre-chamber under inert atmosphere and maintained under vacuum for about 12 h. The residual pressure inside the analysis chamber was less than 1×10^{-9} Torr. The reduced catalysts were prepared in a furnace attached to the XPS instrument, by heating up to 500 °C

($10^{\circ}\text{C min}^{-1}$) under a mixture of 5% H_2 in N_2 for 1 h. First, a long scan was collected; it was used to certify that there was no modification of the peak positions even after long exposition time in vacuum and X-ray beam, necessary to get a reasonable signal-to-noise ratio for all species. Due to the overlap of the Pt 4f and Al 2p peaks, the Pt 4d_{5/2} peak was used to evaluate the concentration and chemical state of the Pt. The binding energies (BE) were referenced to the Al 2s (118.9 eV). The BEs were determined by computational fitting using the CASAXPS (version 2.3.13) software, to an accuracy of ± 0.4 eV. The percentage of Ce^{3+} at the surface of the catalysts was calculated by fitting the Ce 3d XPS signal with 8 components (2 related to Ce^{3+} and 6 related to Ce^{4+}) and making the ratio, following the work of Wang et al. [52] and Meng et al. [53].

Oxygen storage capacity (OSC) was measured using a thermogravimetric analyses (TGA) system (e.g. TA Instruments, SDT Q600 TGA/DSC) following the method described by Wang et al. [54]. The samples were first reduced *in situ* (2.5% H_2/N_2 and total flow of 100 mL min^{-1}) by heating up to 500°C ($10^{\circ}\text{C min}^{-1}$), keeping at this temperature for 1 h. Then, the temperature was decreased to 400°C under H_2/N_2 flow and the flow was alternate (5 cycles) from O_2 (2.5% O_2/N_2 and total flow of 100 mL min^{-1}) to H_2 (2.5% H_2/N_2 and total flow of 100 mL min^{-1}). The mass change (Δm) indicates the oxygen uptake and release capacity of the catalyst. The temperature was decreased down to 100°C , using 100°C steps, and in each step the cycles were repeated. The data were averaged and then converted to OSC [54]. The Pt contribution to OSC was considered similar to all samples, and within this approximation the relative results are presented.

2.3. In situ measurements

X-ray absorption near-edge structure (XANES) and extended X-ray absorption Fine Structure (EXAFS) at Pt L₃-edge (11564 eV) were measured at BM23 beamline of the European Synchrotron Radiation Facility (ESRF), using a Si (111) double crystal monochromator and 0.3 eV energy resolution. Harmonic rejection was obtained using two Si mirrors. The samples were prepared as pellets and placed in a furnace with Kapton® windows [55]. Data was collected in fluorescence mode using a 13 elements Ge detector. The samples were reduced *in situ* by heating up to 500°C under 100 mL min^{-1} $\text{H}_2:\text{He}$ flow (5:95) for 1.5 h and XANES spectra were recorded at 13 min intervals. The sample was cooled down to room temperature under H_2 and EXAFS was measured ($k_{\text{max}} = 13 \text{ \AA}^{-1}$). XANES spectra at Pt L₃-edge under WGS conditions were also carried out for some of the samples. After reduction, the samples were cooled down to room temperature under H_2 where the gas atmosphere for WGS was changed. $\text{H}_2\text{O:CO}$ vol. ratio = 10:1 was used flowing 100 mL min^{-1} of He through a water saturator (22°C , 2.7 mL min^{-1} of steam) and 5.4 mL min^{-1} of 5%CO/He. The vapor pressure in equilibrium was calculated using the Antoine equation [56].

XANES spectra at Ce L₃-edge (5723 eV) were measured at D04B-XAFS1 beamline of LNLS using a Si (111) channel-cut monochromator. The measurements were done in a furnace, designed for transmission mode, during reduction and under WGS conditions. The reduction was done as described before (~ 7 min per spectrum). For the WGS, two $\text{H}_2\text{O:CO}$ vol. ratios were used, 10:1 (as described above) and 3:1. For this, 100 mL min^{-1} flow of 5%CO/He and 50 mL min^{-1} of He passing through a water saturator (65°C) was used to carry steam (15 mL min^{-1}). The samples were heated up to 400°C in steps of 100°C ($5^{\circ}\text{C min}^{-1}$) remaining at each temperature for 1 h.

Ce K-edge (40443 eV) EXAFS were measured at BM23 beamline of ESRF using Si (311) crystal for g-Pt12CeAl and i-12CePtAl and a

furnace for transmission measurements. The samples were reduced under the same conditions described for Pt L₃-edge and XANES were recorded during the heating ramp (~ 11 min per spectrum). EXAFS spectra were recorded at 500°C and at room temperature, after cooling down under H_2/He flow ($k_{\text{max}} = 10 \text{ \AA}^{-1}$). The gas atmosphere was changed for WGS (vol. ratio 10:1), as previously described. The temperature was increased up to 250°C where EXAFS measurements were done.

Details about the XANES and EXAFS data analysis can be found in the support information.

In situ diffuse reflectance infrared Fourier transform spectroscopy (DRIFTS) experiments were carried out using the same equipment described for the FTIR-CO experiments. Prior to the reaction, the catalyst were reduced in 25% H_2/He at 500°C for 1 h and treated with He for 1 h at the same temperature. The background spectra of the catalysts were taken under He flow at the desired reaction temperatures ($200, 250, 300, 350^{\circ}\text{C}$). Finally, the samples were cooled down in He to 200°C and the reactant gas mixture (1%CO and 3% H_2O diluted in He) was fed into the cell. The steam was generated by bubbling He through a saturator containing water at 25°C . The total reactant flow was 100 mL min^{-1} , which correspond to gas hourly space velocity (GHSV) of ca. $0.001 \text{ g min mL}^{-1}$. The sample temperature was raised to 350°C , at 50°C intervals, and the DRIFTS spectra collected. Typically, 128 scans were taken to improve the signal to noise ratio with a resolution of 4 cm^{-1} . The outlet flow was analyzed with a Pfeiffer mass spectrometer.

2.4. Catalytic test

WGS was carried out in a fixed bed quartz reactor (i.d. 9 mm) under atmospheric pressure. Firstly, the samples were reduced at 500°C , for 1 h under H_2 flow of 35 mL min^{-1} . Then, the temperature was decreased to 200°C under He (50 mL min^{-1}) where the reaction mixture was fed into the reactor. Two reaction mixtures were used: 3:1 and 10:1 $\text{H}_2\text{O:CO}$ (vol.). The steam was introduced to the reactor by bubbling He through a saturator containing water at 65°C . For the vol. ratio 3:1 and 10:1, 100 mg and 60 mg of catalyst (100 mesh particles) were used, respectively, diluted with quartz (to complete 200 mg). The ratio between catalyst mass and CO flow was kept constant ($0.02 \text{ g min mL}^{-1}$), which corresponds to total flow rate of 100 and 130 mL min^{-1} for 3:1 and 10:1 ratios, respectively. The outlet gas was analyzed by gas chromatography, employing a GC (Bruker 450) with thermo conductive detector (TCD) equipped with two columns of Porapak N and Molecular Sieve 13X in a series-bypass arrangement. Under operation conditions, heat and mass transfer limitation was negligible as estimated theoretically following standards procedures [57]. The average specific rates ($\text{mol}_{\text{COconv}} \text{ g}_{\text{metal}}^{-1} \text{ s}^{-1}$) were obtained in fixed bed reactor at CO conversion lower than ~ 0.1 at 200°C and ~ 0.2 at 250°C .

3. Results

Table S2 shows the catalysts surface area and CeO_2 crystallite size. The incorporation of Pt-NPs does not significantly affect the textural properties of the $\gamma\text{-Al}_2\text{O}_3$ [49] whereas adding cerium lead to a small decrease in surface area as previously reported [58,59].

Fig. 1a presents the diffraction pattern of PtAl before calcination corresponding to the boehmite precursor. Similar XRD patterns (not shown) were obtained for all sample [51]. Diffraction patterns after calcination are shown in Fig. 1b-f where the broad peaks of the poorly crystallized $\gamma\text{-Al}_2\text{O}_3$ phase could be identified for all samples. Peaks corresponding to CeO_2 fluorite phase ($2\theta = 28.5^{\circ}, 33.3^{\circ}, 47.5^{\circ}$ and 56.4° , marked by * in Fig. 1f) could only be clearly observed in the i-20CePtAl sample, corresponding to a crystalline domain of 5.7 nm (Table S2). In the other

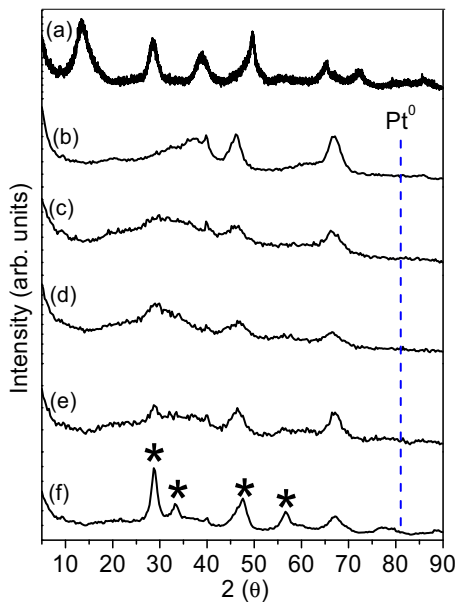


Fig. 1. Diffraction patterns of (a) PtAl (before calcination) and (b) PtAl; (c) g-Pt12CeAl; (d) g-Pt20CeAl; (e) i-12CePtAl; (f) i-20CePtAl after calcination. Peaks marked with (*) correspond to CeO₂ fluorite phase; blue dashed line shows where the (311) Pt peak would appear. (For interpretation of the references to colour in this figure legend, the reader is referred to the web version of this article.)

samples, g-Pt12CeAl, g-Pt20CeAl and i-12CePtAl, the ceria phase lacks long-range order and only a broad feature corresponding to the main peak can be seen indicating that the diameter of the crystalline domains is smaller than 5 nm. However, a careful analysis indicates that ceria crystallinity increases in the order g-Pt12CeAl < g-Pt20CeAl < i-12CePtAl < i-20CePtAl, showing that both higher loadings and the impregnation method facilitate ceria crystallization. Related to the metal phase, the identification of metallic Pt peaks, which would appear if the Pt-NPs agglomerates, is not so straightforward. The first three peaks of Pt⁰ ($2\theta = 39.7^\circ, 46.2^\circ, 67.4^\circ$) are superposed to γ -Al₂O₃ peaks. We found that Pt aggregation

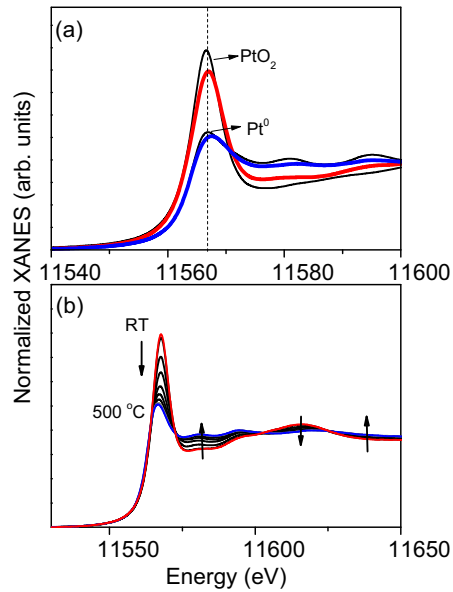


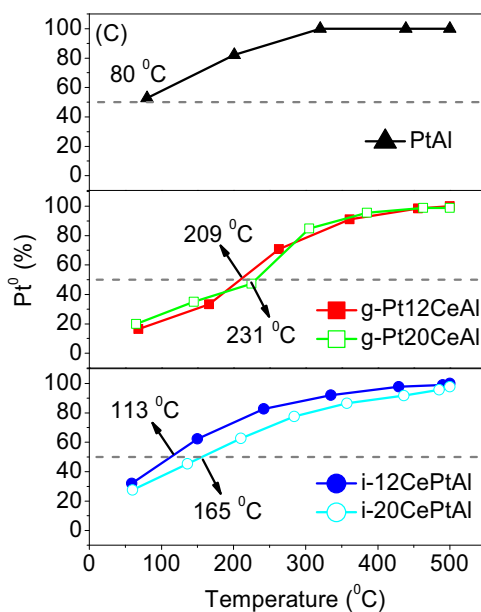
Fig. 2. (a) Pt L₃-edge XANES for i-20CePtAl after calcination (red line) and after reduction (blue line); Pt⁰ and PtO₂ standards are shown for comparison and the dashed line indicates the white line position. (b) *In situ* XANES-H₂ for i-20CePtAl. (c) Evolution of the oxidation state (% Pt⁰) during the reduction: PtAl (black triangles), g-Pt12CeAl (red full squares), g-Pt20CeAl (green empty squares), i-12CePtAl (blue full circles), i-20CePtAl (light blue empty circles). (For interpretation of the references to colour in this figure legend, the reader is referred to the web version of this article.)

could be better confirmed by also evaluating the region at higher angles, by the analysis of the (311) Pt peak at $2\theta = 81.2^\circ$ (indicated by the dashed line in Fig. 1) [49]. The clear lack of this reflection is an indication that the Pt-NPs were well dispersed in all samples, as described previously [49,50].

Fig. 2a shows the Pt L₃-edge XANES of i-20CePtAl in comparison with the Pt and PtO₂ standards (the data for the other samples are similar and not shown). The Pt-NPs became partially oxidized during the calcination process, as evidenced by the intensity of the white line, indicated by the dashed line in Fig. 2a. By heating under H₂, the total reduction of the Pt-NPs is achieved at about 500 °C. The final spectrum does not fully correspond to the standard due to size effects and temperature. *In situ* XANES during reduction (XANES-H₂) is shown in Fig. 2b for this sample. Isosbestic points can be seen, showing that the transition from the oxidized to the metallic phase occurs without intermediate species and the Pt-NPs are fully reduced after this process. Fig. 2c shows the evolution of the Pt oxidation state during the reduction for all samples. The first point in Fig. 2c corresponds to the samples just after the calcination and it can be seen that the PtAl is less oxidized (53% Pt⁰) than the samples containing Ce. Comparing the samples containing Ce, the GEL samples are more oxidized (16 and 20% Pt⁰ for g-Pt12CeAl and g-Pt20CeAl, respectively) than the IMP samples (32 and 27% Pt⁰ for i-12CePtAl and i-20CePtAl, respectively). As mentioned before, the PtAl sample is ~50% reduced after calcination (*i.e.*, 50% Pt⁰) while for the samples with Ce, the temperature needed to achieve this degree of reduction was 209 °C for g-Pt12CeAl, 231 °C for g-Pt20CeAl, 113 °C for i-12CePtAl and 165 °C for i-20CePtAl. In addition, PtAl is completely reduced at 321 °C while the samples containing Ce reduce only at 500 °C.

Fig. 3 presents the Pt L₃ edge EXAFS and the best fits for PtAl after the reduction (g-Pt12CeAl and i-12CePtAl are presented in Fig. S2). Damped coordination shells above 3 Å are observed, as expected for nanoparticles (Fig. 3). EXAFS results after the reduction are shown in Table 1 and are very similar among samples after reduction, independently of the Ce presence or incorporation method.

FTIR-CO and XPS were performed to obtain complementary information about the catalysts surface. While FTIR-CO provides



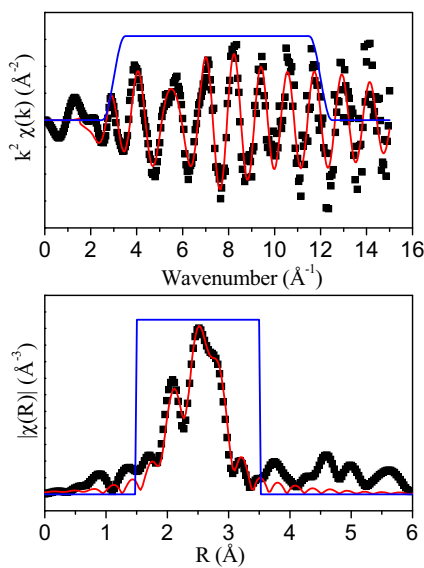


Fig. 3. Pt L₃-edge EXAFS data of PtAl after reduction at room temperature, best fit in k space (above) and magnitude of the Fourier transform (below). Black squares (data); red line (fit) and blue line (window). (For interpretation of the references to colour in this figure legend, the reader is referred to the web version of this article.)

Table 1

Pt L₃-edge EXAFS results for PtAl, g-Pt12CeAl and i-12CePtAl samples after reduction. Data for Pt foil (standard) is also shown for comparison.

	PtAl	g-Pt12CeAl	i-12CePtAl	Pt standard
N _{Pt-Pt}	6.5 (±0.6)	6 (±1)	6 (±1)	12
R _{Pt-Pt} (Å)	2.75 (±0.01)	2.76 (±0.01)	2.75 (±0.01)	2.76 (±0.02)
σ ² _{Pt-Pt} (Å ²)	0.006 (±0.001)	0.009 (±0.002)	0.007 (±0.002)	0.004 (±0.003)

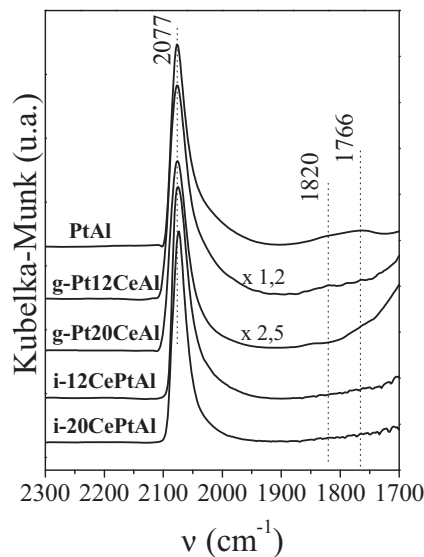


Fig. 4. FTIR-CO of the catalysts after reduction. The multiplication factors are indicated and used for clarity.

indirect information about the exposed Pt sites and Pt electronic density through the modification of CO stretching bands (linear, bridge, 3-fold), XPS provides direct information on the surface chemical composition and electronic state. FTIR-CO measurements were collected in the 2300–1700 cm⁻¹ region, shown in Fig. 4. In the high wavenumber region (2200–2000 cm⁻¹) all spectra exhibit a main band at about 2077 cm⁻¹, assigned to CO linearly bonded to high coordination Pt sites [60] and a tail at low frequencies. The

Table 2

BEs for Pt 4d_{5/2}, atomic surface composition and % of Ce³⁺ after calcination (C) and after (R) reduction.

Samples	Pt 4d _{5/2}	BE (eV)	%Concentration		%[Ce ³⁺]	
			Pt	Al	Ce	—
PtAl	C	315.1	60.4	0.1	39.5	---
	R	314.6	57.5	0.1	42.4	---
g-Pt12CeAl	C	316.0	60.6	0.1	38.0	1.2
	R	315.1	57.6	0.1	40.9	1.4
g-Pt20CeAl	C	315.8	58.8	0.1	39.1	2.0
	R	315.3	57.9	0.1	39.9	2.0
i-12CePtAl	C	315.6	59.6	0.1	39.4	0.8
	R	314.8	60.1	0.1	38.9	1.1
i-20CePtAl	C	316.2	63.8	0.1	34.8	1.3
	R	315.1	60.9	0.1	37.4	1.6

*BE for Pt⁰ = 313.6 eV and PtO₂ = 316.8 eV [49].

main band at 2077 cm⁻¹ shows a slight red shift for the catalysts promoted by ceria, but is within experimental error (4 cm⁻¹). It is known that lateral interactions can significantly shift band positions [61], but detailed studies have also associated the signal in the ~2050–2010 cm⁻¹ region with the adsorption of CO on smaller Pt NPs or Pt defects sites (corners and edges) in a linear mode [62–66]. It is worth to note that the PtAl catalyst also show in the low wavenumber region, a pair of overlapping bands at 1820 and 1766 cm⁻¹. The band at 1820 cm⁻¹ is associated with CO bonded to two Pt atoms in bridge form whereas the band at 1766 cm⁻¹ is assigned to CO bonded to Pt species in tridentate mode [62]. In the presence of ceria, the adsorption of these species, become unfavorable due to the decrease of the Pt electronic density or the presence of patches of ceria on the Pt surfaces [50,62].

XPS measurements were performed after calcination (C) and after reduction (R). The results are shown in Table 2 and the spectra can be found in Figs. S3 and S4. All calcined samples present Pt 4d_{5/2} BEs closer to PtO₂ (316.8 eV) than Pt⁰ (313.6 eV) [49]. These high BEs confirm partial oxidation of the Pt-NPs during catalyst preparation and/or an important interaction with the support. The XPS results are in agreement with the XAFS data presented before. After reduction, all samples present a slight decrease in the Pt 4d_{5/2} BEs but the values are still higher than the BE of the metallic Pt. This effect is more pronounced in the ceria-promoted catalysts, in agreement with Riguette et al. [62].

The surface atomic compositions are similar for all catalysts, according to Table 2. The Pt surface concentration is quite small and corresponds to about 12% of the total Pt concentration. This was expected considering that the Pt-NPs are embedded in the oxide matrix. A slight variation of Ce surface concentration was found when comparing GEL and IMP samples of same bulk concentration (12 or 20%). In general, the IMP samples show smaller Ce surface concentrations, compared to the corresponding GEL samples, which is in accordance with the stronger segregation and crystallization of CeO₂ in the IMP catalysts, as indicated by XRD in Fig. 1. The reductive treatment leads to a slight increase of Ce surface concentration for most of the samples. The atomic percentages of Ce³⁺ at the surface are also presented in Table 2. The results confirm the partial reduction of Ce⁴⁺ to Ce³⁺ after H₂ treatment at 500 °C.

To get a deeper insight into the properties of the cerium oxide phase, XAFS spectra at Ce L₃-edge were collected. Fig. 5a shows the initial spectrum of the calcined g-Pt20CeAl and the best fit. The most pronounced features (C and D for this sample) are characteristic of CeO₂ and the slight difference in the relative intensities compared to the bulk standard (Fig. 5b) are probably related to nanometric effects. The fit results for the standards are shown in

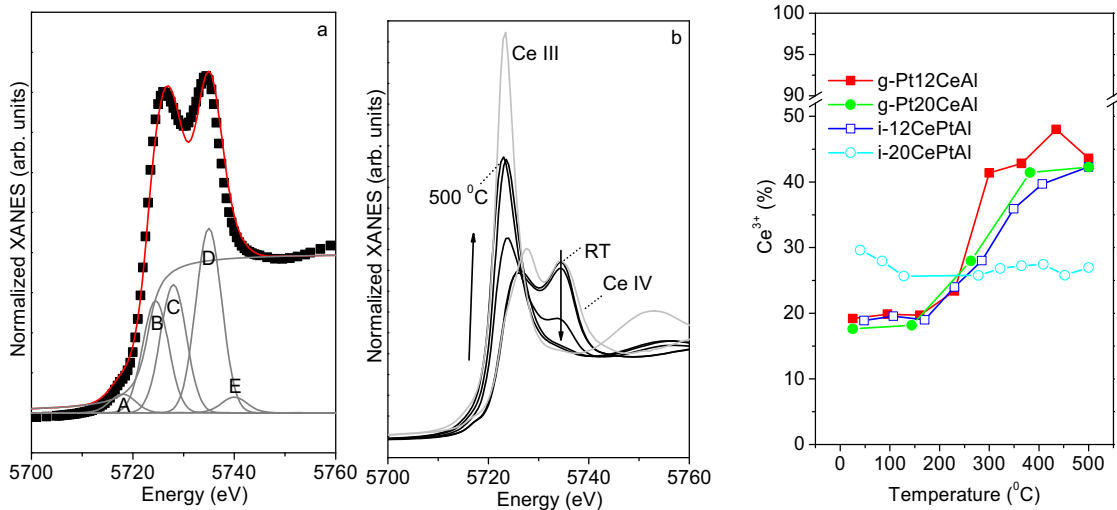


Fig. 5. (a) Ce L₃-edge XANES for the calcined g-Pt20CeAl (squares) and the best fit (red line) obtained by the sum of Gaussians and Arctan functions, associated to Ce electronic transitions (gray curves). (b) *In situ* XANES-H₂ at Ce L₃-edge for g-Pt20CeAl, standards are shown in gray for comparison. (c) Evolution of the cerium oxidation state (as Ce³⁺) of the catalysts during reduction. (For interpretation of the references to colour in this figure legend, the reader is referred to the web version of this article.)

Fig. S1. Fig. 5b shows the spectra evolution during reduction for g-Pt20CeAl catalyst (similar for the other ones). By increasing the temperature under H₂, the features C and D decrease and feature B increases, corresponding to the transition from Ce⁴⁺ to Ce³⁺ [67]. The evolution of the cerium oxidation state (as Ce³⁺) for all catalysts is shown in Fig. 5c. At the beginning, all the samples have about 20% of Ce³⁺ except for i-20CePtAl that presents about 30%, probably due to the formation of larger crystallite size and species that are not easily reduced (as observed by XRD, Fig. 1). Samples g-Pt12CeAl, g-Pt20CeAl and i-12CePtAl present similar behavior and at the end of the reduction the amount of Ce³⁺ increases to 42%. The sample with the larger CeO₂ crystalline domain, i-20CePtAl, does not significantly change its overall oxidation state.

Ce K-edge EXAFS was performed for g-Pt12CeAl and i-12CePtAl after calcination, under H₂ at 500 °C, and after cooling down under H₂ at room temperature. EXAFS data under WGS at 250 °C were also obtained. Fig. 6 presents the magnitude of the Fourier transform at the Ce K-edge for each catalyst after calcination and after reduction. The contributions used in each fit are also indicated in Fig. 6 and fit results are presented in Table 3. EXAFS data and corresponding fits for these two samples under all conditions are presented in Fig. S5 and the results are presented in Table S3.

From the structural parameters presented in Table 3, it is possible to observe that both samples show a significant attenuation of the oscillations compared to the CeO₂ standard due to the small crystallite size and/or higher degree of disorder. Comparing both samples, i-12CePtAl is clearly more ordered than g-Pt12CeAl since the Ce-Ce contribution is visible at ~3.8 Å (but with N_{Ce-Ce} much smaller than the CeO₂ standard). For the CeO₂ standard, the first coordination shell corresponds to 8 O neighbors at 2.34 Å [ICSD Coll Colde: 156250]. For the samples, however, it was necessary to include two Ce-O contributions, one at about 2.25 Å and another at 2.40 Å, that indicate that Ce bounds to different species at the surface or at the interface with alumina. After reduction, the Ce environment seems to become more disordered and a Ce-Al contribution (3.27 Å) appears.

Several works have proposed that ceria OSC impacts directly the catalytic activity by facilitating the water activation [8,16,68]. Aspects that may enhance or reduce the ceria OSC are: ceria surface area [69], contact between the metal and the ceria [70,71], crystallographic orientation and defects. It has been proposed that oxygen is more easily removed from high defect surfaces and small

crystallites [69,72]. For both set of samples, GEL and IMP, the OSC increases with the Ce-loading (73 and 116 μmol O₂·g_{catalyst}⁻¹ for the g-Pt12CeAl and g-Pt20CeAl, and 79 and 92 μmol O₂·g_{catalyst}⁻¹ for i-Pt12CeAl and i-Pt20CeAl, respectively; at 300 °C). Interesting, comparing the samples prepared by the same method, the smaller amount of ceria (12%wt) leads to higher OSC per g_{CeO₂}.

Fig. 7 shows the catalytic results under WGS as a function of temperature for H₂O:CO ratios of 10:1 and 3:1. Overall, the samples show activity above 200 °C and the presence of cerium increases the CO conversion for both H₂O:CO ratios.

WGS specific reaction rate results are presented at Table 4. The presence of Ce increases the specific reaction rate in all samples, by a factor up to seven compared to PtAl, depending strongly on the ceria contents and temperature. It becomes clear that ceria plays a more important role at 250 °C. The increase of cerium from 12 to 20 wt%, for both set of samples (GEL and IMP) and both H₂O:CO ratios, roughly doubles the specific reaction rate. In addition, increasing the H₂O:CO ratio from 3:1 to 10:1 has a similar effect since the reaction order is positive to water and larger than the reaction order to CO, for the reaction over a Pt surface [3,26]. It is important to remark that the specific reaction rates and turnover frequencies values are significantly affected by the reaction conditions, metal dispersion and metal-support interaction and several values can be found in the literature [9,26,27].

Considering the structural characterization under WGS reaction conditions, no changes with respect to the corresponding reduced samples are observed at the Pt L₃-edge XANES (not shown). Also, no modifications of the Ce environment under WGS are detected by Ce K-edge EXAFS (Table S3, Fig. S5). The quantification of Ce³⁺ from Ce L₃-edge XANES taken at 300 °C is shown in Table 5 (within 5% estimate error). Similar values are found for the measurements done at 200, 300 and 400 °C. For H₂O:CO = 10:1, g-Pt12CeAl and g-Pt20CeAl are more reduced under WGS than at the end of the reduction, i-12CePtAl is more oxidized and i-20CePtAl remains constant. On the other hand, for H₂O:CO = 3:1, the GEL samples are more oxidized while i-12CePtAl is more reduced. Therefore, no straightforward trend could be found among the samples. The constant oxidation state of Ce under reaction conditions at different temperatures, similar to what happened to Pt, indicates that only modifications at the surface might be happening with the temperature, not detected in these measurements.

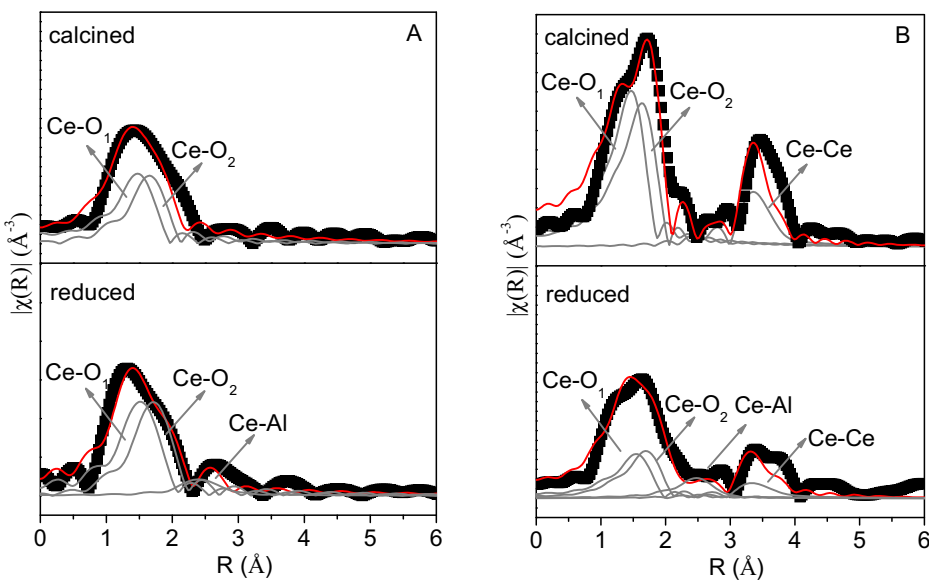


Fig. 6. Magnitude of the Fourier transforms and best fits for (a) g-Pt12CeAl (b) i-12CePtAl, after calcination and after reduction (Ce K-edge). Data collected at room temperature. The main contributions to the fits are indicated by the gray lines. See Table 3 and text for details.

Table 3

Structural parameters obtained by the Ce K-edge EXAFS analysis of g-Pt12CeAl and i-12CePtAl after calcination and after reduction (measurements at RT).

	Calcined		H_2 25 °C		CeO ₂
	g-Pt12CeAl	i-12Ce PtAl	g-Pt12CeAl	i-12Ce PtAl	
ΔE_0	-4 ^a	-4 ^a	-4 ^a	-4 ^a	-4 (± 2)
S_0^2	1 ^a	1 ^a	1 ^a	1 ^a	1 (± 0.2)
$N_{\text{Ce}-01}$	3.1 (± 0.2)	3.9 (± 0.4)	3.9 (± 0.3)	3.5 (± 0.4)	8
$R_{\text{Ce}-01}$ (\AA)	2.23 ^b (± 0.03)	2.23 ^b (± 0.03)	2.28 ^b (± 0.03)	2.28 ^b (± 0.03)	2.34 (± 0.02)
$N_{\text{Ce}-02}$	3.0 (± 0.3)	5.7 (± 0.5)	5.1 (± 0.4)	4.3 (± 0.5)	-
$R_{\text{Ce}-02}$ (\AA)	2.43 ^c (± 0.06)	2.43 ^c (± 0.06)	2.47 ^c (± 0.04)	2.47 ^c (± 0.04)	-
$N_{\text{Ce}-\text{Al}}$	-	-	2.7 (± 0.7)	2.0 (± 0.8)	-
$R_{\text{Ce}-\text{Al}}$	-	-	3.20 ^d (± 0.03)	3.20 ^d (± 0.03)	-
$N_{\text{Ce}-\text{Ce}}$	-	5 (± 1.5)	-	3.8 (± 1.5)	12
$R_{\text{Ce}-\text{Ce}}$ (\AA)	-	3.86 (± 0.03)	-	3.86 (± 0.05)	3.85 (± 0.02)
σ^2 (\AA^2)	0.005 ^e (± 0.001)	0.005 ^e (± 0.001)	0.010 ^e (± 0.006)	0.010 ^e (± 0.006)	0.005 (± 0.002)

^a Fixed values and equal to CeO₂ standard.

^b $R_{\text{Ce}-01}$ was constrained to be equal for the calcined and reduced samples of the same catalyst.

^c $R_{\text{Ce}-02}$ was constrained as in^b.

^d $R_{\text{Ce}-\text{Al}}$ was constrained as in^b.

^e σ^2 was constrained as in^b.

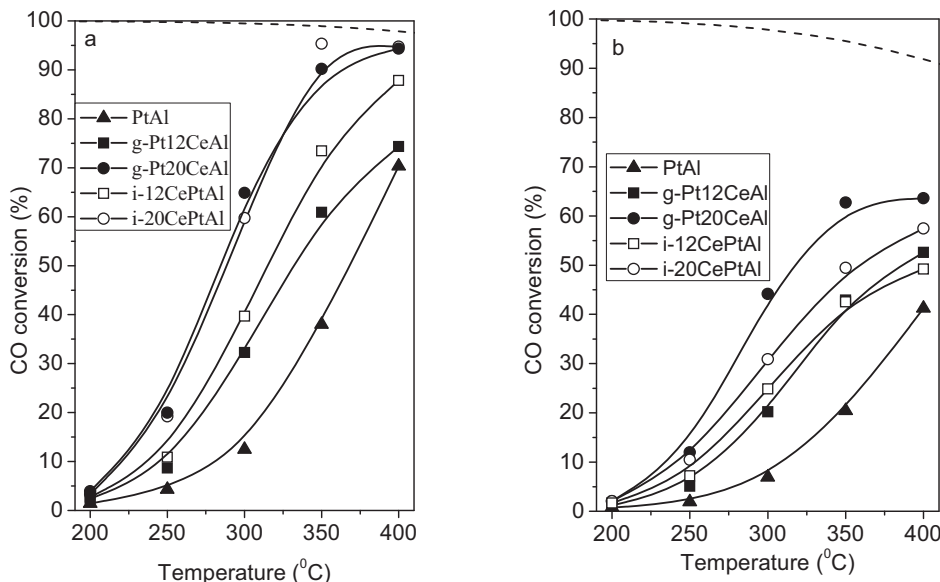


Fig. 7. Catalytic test for $\text{H}_2\text{O}:\text{CO}$ ratios of (a) 10:1 and (b) 3:1. The dashed lines in both graphics correspond to the thermodynamic limit.

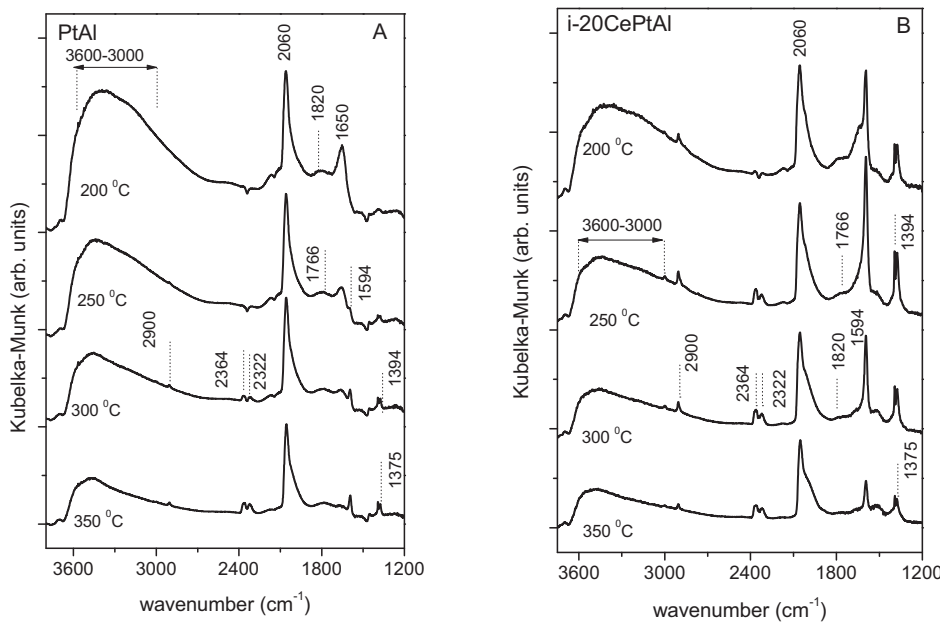


Fig. 8. DRIFT spectra of PtAl (A) and i-20CePtAl (B) catalyst during WGS reaction at different temperatures.

Table 4

WGS average specific reaction rates ($\text{mol}_{\text{COconv}} \text{g}_{\text{metal}}^{-1} \text{s}^{-1}$) at 200 and 250 °C for both $\text{H}_2\text{O}:\text{CO}$ ratios.

Samples	Rate at 200 °C ($\times 10^5$)		Rate at 250 °C ($\times 10^5$)	
	10:1	3:1	10:1	3:1
PtAl	3.9	2.3	13	5.7
g-Pt12CeAl	7.2	3.6	28	16
g-Pt20CeAl	12	6.2	75	42
i-12CePtAl	8.3	5.1	36	23
i-20CePtAl	10	6.3	71	36

Table 5

Ce^{3+} (%) under WGS obtained from XANES analysis at Ce L₃-edge.

	%Ce ³⁺	
	$\text{H}_2\text{O}:\text{CO} = 10:1$	$\text{H}_2\text{O}:\text{CO} = 3:1$
g-Pt12CeAl	55	35
g-Pt20CeAl	45	25
i-12CePtAl	38	47
i-20CePtAl	26	— ^a

^a Not measured.

To probe the evolution of surface species during WGS, *in situ* DRIFTS was performed. Under reaction conditions, vibrational modes of hydroxyls (3600–3000 cm⁻¹), formates (2900 cm⁻¹, 1650–1350 cm⁻¹), carbonates and carboxylates (1700–1000 cm⁻¹), as well as Pt-CO bands (2100–1950 and 1820–1766 cm⁻¹) are observed for all samples [15]. These bands are presented in Fig. 8 for PtAl (A) and i-20CePtAl (B). A set of similar bands to i-20CePtAl is observed for the other samples containing cerium (Fig. S6). The band at about 2060 cm⁻¹ is assigned to the CO adsorption on Pt sites in the linear mode. Compared to FTIR-CO (Fig. 4), this band is significantly shifted under reaction conditions mainly due to the higher temperature (> 200 °C) and consequently lower CO coverage fraction (of about $\theta_{\text{CO}} = 0.27$, see Fig. S7). In addition, under reaction, besides CO, other species such as H, O and OH might be adsorbed at the Pt surface [45]; these species are predominantly σ bonded and would decrease the electronic density at Pt surface contributing to the band shift to lower frequencies.

The overall widths of the CO adsorption bands are also slightly broader under WGS compared to FTIR-CO experiments (Fig. 4). As in the case of FTIR-CO measurements (Fig. 4), there are other two bands in the low frequency region (1820 and 1766 cm⁻¹) for the PtAl sample (Fig. 8A). These bands remain constant even with the temperature increase. On the other hand, these bands are not clearly observed for the i-20CePtAl under CO atmosphere (Fig. 4) but are observed under reaction conditions at 200 °C. This indicates that the formation of Ce-O-Pt adducts, which hinders the adsorption of CO multi-coordinated, is apparently less effective under reaction conditions. Furthermore, in the i-20CePtAl, these bands wash out by increasing the temperature.

The broad band at 3600–3000 cm⁻¹ confirms the presence of asymmetric and symmetric stretching of OH vibration of water molecules on the surface. Bands associated with formates and carbonates species are clearly observed for i-20CePtAl at 1594, 1394 and 1375 cm⁻¹ [15]. In addition, a low intensity pair of bands is observed at around 2900 cm⁻¹, which confirms the presence of CH bond associated to formates. For PtAl, these bands appear just above 300 °C. Thus, the cerium presence leads to the formation of formates at the catalyst surface at low temperatures. For i-20CePtAl, above 250 °C the appearance of adsorption modes of CO₂ in 2364 and 2322 cm⁻¹ confirms the progress of the WGS reaction. For PtAl, this set of band appears above 300 °C confirming the higher reactivity for the samples with Ce as observed for the catalytic test. At 350 °C there is a decrease in the intensity of symmetric and asymmetric stretching modes of water, suggesting desorption of these species at higher reaction temperature.

For i-20CePtAl there is an increase in intensity of the bands at 1594 and 1394 cm⁻¹ with increase of temperature from 200 to 250 °C (Fig. 8B). This result indicates the CO oxidation forming stable formates and carbonates that accumulate on the surface. At 300 °C there is a decrease in the intensity of formates bands at 2090 and 1594 cm⁻¹, suggesting the decomposition of these species at higher reaction temperature, while for PtAl catalyst this species seems stable at higher temperature.

To get further information on the interaction of CO in the absence and presence of water, the samples were subsequently analyzed by closing and opening the water inlet at 350 °C, after being submitted to WGS conditions. Fig. 9 shows the results for the

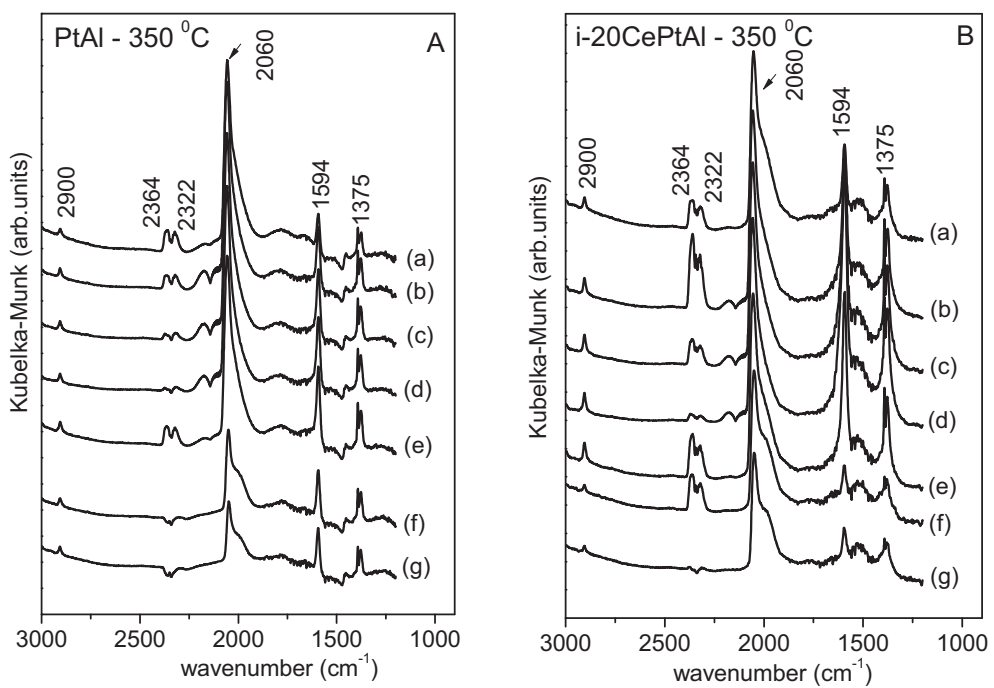


Fig. 9. DRIFT spectra for PtAl (A) and i-20CePtAl (B) catalysts at 350 °C under (a) WGS (CO + H₂O + He), under CO + He for (b) 1 min, (c) 5 min, (d) 10 min; under WGS again after (e) 1 min and output and feeding closed for (f) 10 min and (g) 15 min.

samples PtAl (A) and i-20CePtAl (B). While CO₂ bands (2364 and 2322 cm⁻¹) decrease with time in the absence of water, formate and carbonate (2900, 1594 and 1375 cm⁻¹) and Pt-CO (2060 cm⁻¹) bands remain almost constant. The results demonstrate that in absence of H₂O (Fig. 9 A-b,c,d and B-b,c,d), formates accumulate by CO oxidation on both supports, alumina and ceria-alumina, and are very stable [73]. The water is turned on again and the CO₂ band reappear at the surface (Fig. 9A-e and B-e).

To analyze the stability of species on the surface, the feeding was interrupted and the spectra recorded at 350 °C after 10 and 15 min. Complete CO₂ desorption is observed after 10 min for PtAl and after 15 min for i-20CePtAl, while the formate band at 1564 cm⁻¹ decreases but it is still present.

4. Discussion

By preparing the catalysts from the same batch of colloidal nanoparticles it was possible to obtain Pt-Al₂O₃ and Pt-CeO₂-Al₂O₃ catalysts with similar platinum dispersion as previously described [49,50]. This strategy of synthesis allowed evaluating independently and in an uncorrelated manner the impact of the structural and redox properties of the CeO_x on the alumina support in the WGS reaction. By changing the method used to produce the ceria-alumina support it was possible to raise interesting questions about the impact of support properties and its interaction with the metal particles.

XANES and XPS results show that the supported Pt-NPs oxidize during catalyst sol-gel preparation and calcination, which can be reversed by reduction. After reduction, the Pt-NPs in all catalysts show similar structural parameters, confirmed by EXAFS.

Since the Pt-NPs are similar in all samples, a similar standard free energy and equilibrium constant for the Pt + O ⇌ PtO reaction could be expected. Nevertheless, clear differences among the catalysts were found. Before reduction, the Pt-NPs are more oxidized on samples containing ceria; among the ceria containing samples, the GEL samples lead to higher Pt-NPs oxidation. Theoretical calculations [74] show a charge transfer when Pt is on top of CeO₂ (111)

surface with spontaneous reduction of the substrate and formation of vacancies, changing the cerium oxidation state in the vicinity of Pt from Ce⁴⁺ to Ce³⁺. The more severe oxidation observed for GEL samples suggests that the Pt–O–Ce interaction is more extensive when Ce is added to gel. Additionally, for the GEL samples higher temperatures are necessary to reach the same amount of Pt⁰ and PtO₂ (Fig. 2b) reinforcing the difficulty in reducing Pt in the presence of Ce. Higher reduction temperature was also observed by González et al. [6] comparing Pt/CeO₂ with Pt/TiO₂ or Pt/CeO₂-TiO₂, which was assigned to differences in the metal-support interaction. The higher temperature found for Pt on CeO₂ was attributed to the reduction of PtO_x species while the lower temperatures on TiO₂ and CeO₂-TiO₂ would be due to the reduction of PtO_x with lower stoichiometry (PtO).

After reduction, Pt-NPs show similar structural parameters (Table 2) and it is not possible to see differences in the average oxidation state of the Pt-NPs by *in situ* XAFS (Fig. 2b); however, XPS results suggest partial Pt surface oxidation and/or charge transfer to the support. Interestingly, FTIR-CO spectra were sensitive to the presence of Ce through the relative intensity and symmetry of the bands. Additionally, bands in the low wavenumber region of the IR spectra (Fig. 4) are strongly suppressed in Ce-promoted catalysts; these results indicate that ceria may change the local Pt electron density or block part of the Pt sites [62,65,66].

Many factors influence the support and metal-support interaction. In our case, considering the similarity among the samples concerning the Pt-NPs, the support characteristics and its interface with Pt should mainly determine the catalyst properties. Different Ce species could be expected based on the preparation methods and conditions: i) crystalline CeO₂ and non-stoichiometric phases; ii) few nm-sized CeO₂ crystallites and/or a highly dispersed CeO_x phase that could not be detected by XRD; and iii) Ce-O-Al local surface sites.

The results show that the GEL preparation method and smaller loading favor the formation of a more dispersed phase. In fact, only for the i-20Ce PtAl the XRD pattern of nanocrystalline CeO₂ domains can be clearly recognized. This reflected on cerium oxida-

tion state, and in this aspect, this sample is differentiated, showing smaller% of Ce³⁺ (surface and bulk) that is not significantly affected by reduction at 500 °C.

Looking in more detail at the local structure of the ceria phase, the Ce K-edge EXAFS analysis reveal some interesting features. It confirms that the IMP samples have a more ordered structure than the GEL samples. In particular, the i-12CePtAl sample shows a Ce–Ce contribution with average distance similar to the CeO₂ phase; this contribution is not presented in the g-Pt12CeAl. Different from the bulk CeO₂, however, two Ce–O distances are found for both samples, one shorter (~2.23–2.28 Å) and another longer (~2.43–2.47 Å) than the CeO₂ fluorite phase (2.34 Å). Similar Ce–O distances were previously reported in the literature: the shorter one was found in 4-fold Ce³⁺sites in (111) CeO₂ (short distance) [75] and the long one in surface sites of nanometric Ce₂₁O₄₁ [75], in Ce₂O₃ [ICSD Coll.Code: 96202], and in CeAlO₃ [ICSD Coll.Code: 150277]. Interesting, after reduction a Ce–Al contribution is detected, independently of the preparation method. The Ce–Al distance is similar to the one found in CeAlO₃. It is important to remark, however, that is unlike that the crystalline CeAlO₃ would be formed at the low temperatures used in this work (maximum of 500 °C) [76]. In fact, both EXAFS and XRD data show that the formation of CeAlO₃ crystalline phase is ruled out. The results also show that Ce₂O₃ crystalline phase is not formed under reduction. In these two phases, the Ce–Ce distance would be longer (4.08 Å) and shorter (3.27 Å), respectively. Therefore, although we detect small crystallites of CeO₂ in the IMP catalysts, it is likely that in all samples a large fraction of a well dispersed CeO_x phase is formed and that the reduction enhances the interaction with the alumina support.

Ceria structure is intrinsically related to the amount of Ce³⁺ and vacancies formation. Vacancies formation is easier in small CeO₂ particles than on CeO₂ surfaces and it is further facilitated by the presence of Pt [40,68,77–79]. Migani et al. [78] demonstrated that the energy separation between the valence and the conduction band for ceria nanoparticles is lower compared to the (111) surface, promoting vacancy formation. The addition of metallic Pt-NPs favors the formation of Ce³⁺ ions by electron transfer from the metal cluster. Thus, the vacancy formation also depends on the contact between the removed O and Pt [77]. Concerning ceria crystallographic orientation, earlier studies proposed a high OSC for the (100) surface when compared to (110) or (111) since the energy required to form an oxygen vacancy is smaller [80,81]. Further experimental observations and DFT analysis stated that oxygen vacancies tend to group together in clusters [82]. Thus, it is possible to observe that ceria vacancy formation and as a consequence the OSC depends on its interaction with alumina, its particle size, its surface structure and its proximity to a metallic nanoparticle and as a consequence, should be deeply affected by the catalyst preparation method. In our case, the OSC results are an average contribution of several species and the weight of each one varies among the samples. The similar OSC values found for samples with the same ceria content, despite the larger average CeO₂ crystalline domain in the IMP samples suggest that small CeO₂ particles distribution tail and highly dispersed CeO_x species dominates.

Considering the WGS activity, regardless the debate about the dominant mechanism (redox, associative or associative with redox regeneration) and the most likely intermediates (formate, carbonate, carboxylate), it is a consensus that ceria and its interface with Pt play an important role in water activation and the intermediates that are formed [14,27,83]. While CO is only activated on the metal, water can be activated on Pt, on the support or on the metal–support interface [27,29,37,39,41].

The participation of formates as intermediates has been intensely discussed in the literature, and one of the reasons is the difficulty in associate the FTIR date with kinetics data in different temperatures and compositions [84,85]. A critical analysis

of contribution of formate mechanism was presented by Burcha et al. [25], concluding that formates account for just a small percentage of the total WGS reaction. Jacobs et al. [73], on the other hand, raised several arguments in favor of the intermediate role played by the formates, in particular at low temperature WGS conditions, since assistance of water is critical to formates decomposition under reaction. A recent work using concentration-modulation spectroscopy in DRIFT mode under WGS reaction at low temperature 250 °C showed that the absorption bands from carbonate (1500–1400 cm⁻¹) and bidentate formate (1550, 1370 cm⁻¹) groups vanish in the phase-resolved spectra, indicating that they are spectator species [15]. On the other hand, the monodentate formate and carboxylate species are found to be intermediates, in agreement with carboxyl mechanism activated at the metal–oxide interface. Concerning the role of carbonates, evidences of their high stability on Pt/CeO₂ at 300 °C was obtained using transient isotopic experiments, where is excluded the exchanges of carbonyl in ¹²CO₃²⁻ with ¹³CO in gas phase [23]. The participation of labile oxygen of the ceria support in the WGS reaction supporting the redox mechanism was demonstrated using ceria as source of ¹⁸O and monitoring the evolution of C¹⁶O₂, C¹⁶O¹⁸O₂ and C¹⁸O₂ with time on stream. The dependence of the activity with ceria structural properties and nanosize effects were not addressed in this work.

It is clear that the samples studied in this work have significant differences related to the balance of the different CeO_x species and its initial interaction with the Pt-NPs. Surprisingly, the results do not pointed out a direct correlation with the performance in WGS. Panagiotopoulou and Kondarides [86] found that for Pt/CeO₂ catalysts, with CeO₂ particles in the size range of 10–21 nm and surface areas of 25–57 m²/g, the catalytic activity did not depend on the structural and morphological characteristics of CeO₂. However, recent theoretical studies by Vayssilov et al. [40] found that the oxygen transfer from ceria to Pt (reverse oxygen spillover) is strongly dependent on the ceria structure at nanoscale and its contact with Pt and can help to explain the enhanced performance of Pt–CeO₂ catalysts. Therefore, it could be expected that the smaller crystalline domains and the clear different characteristics among our samples should affect the activity, in agreement with the work by Bunluesin et al. [87]. In addition, the existence of a reactive zone around the Pt-NPs in WGS reaction, in the order of 1–2 nm for ceria-based supports has been discussed in several works [17–23,37,73], and is dependent, for example, on the presence of dopants, such as Ti⁴⁺, La³⁺ and Zr⁴⁺ [20,23]. The diffusion of the intermediates species in this reaction zone is a key aspect that affects the reaction rate. It could be expected that ceria nanosize effects have a significant impact.

Several works have pointed out a dependence of the WGS activity on Pt particle size (or Pt loading) and support [17,23,29,46]. In our case, the Pt-NPs size are similar among the samples, but the ceria phase was different. In fact, the electron density changes on Pt surface through the position of adsorbed CO band or contraction of Pt–Pt distance bond could not be clearly observed in different catalysts. Thus, it could be reasonable to suggest in a first approximation a similar catalytic property for Pt sites in PtAl and PtCeAl. It has been presented in the literature [23] that turnover frequencies in Pt/CeO₂ catalysts do not strongly depend on the Pt size, for particles in the ~1–8 nm range. On the other hand, it has been proposed that the interfacial Pt–O–Ce sites are the most reactive [23,29,88,89].

It is interesting to mention that several works also point out that the strong metal support interaction, especially found in small Pt particles in contact with ceria, is determinant to the reaction pathway, mainly influencing water activation and dissociation [27,29]. The Pt–O–Ce interaction, as demonstrated from theoretical studies [29], significantly enhances the ability of the admetal to adsorb water and dissociate the O–H bonds. It also affects the stability and decomposition of intermediates [27,73]. Aranifard et al. [27]

demonstrated from first principle that the Pt–O–Ce interface sites are 2–3 orders of magnitude more active than Pt(111) and the associative carboxyl pathway with redox regeneration could be the preferential pathway to the overall rate. Our experimental data showed that for Ce-containing catalysts the WGS specific reaction rates increase less than one order of magnitude compared to the PtAl unpromoted catalyst, lower than expected based on the theoretical studies (about 2 orders of magnitude taking in account the way Pt atoms are considered, surface or perimeter) [27]. On the other hand, theoretical calculations showed a decrease in the density of Pt 5d states near the Fermi level for the Pt/CeO₂(111) system compared to bulk Pt [90,91], in agreement with our XPS data. Thus, a smaller heat of adsorption of CO bonded on Pt atoms is expected at the Pt–O–Ce interface, increasing the reactivity of the CO interface relative to the unpromoted catalyst. Compared to the PtAl, the changes of electron density of Pt near the Pt–O–Ce interface and the presence of Pt–O–Ce could increase the reactivity of CO and enable a new pathway for WGS, respectively. Considering that, (i) at high WGS temperature a small fraction of the Pt surface is covered by CO (Fig. S7), (ii) not all adsorbed CO are part of the active pool [23], (iii) formates and carbonates are stable species; (iv) not all Pt sites make interface with ceria; and (v) different ceria species exist in our samples; the main dependence of the activity with the two ceria loading for the two preparation methods, and not with the average ceria structural properties, suggests that the creation of the interfacial sites seems to be the limiting factor in these samples. Therefore, increasing the cerium loading is likely to increase the amount of most active sites at interface of Pt interacting with ceria.

5. Conclusion

Catalysts are very complex and dynamic systems since their behavior depends on the structural and electronic properties of different species and on the temperature and atmosphere they are submitted to. In this work we show that the presence of Ce in PtAl catalysts increases the WGS specific reaction rates up to seven times in the WGS reaction. Several parameters impact the activity and the use of pre-formed Pt-NPs was the strategy adopted to prepare model systems focusing on the support and interface effects. It was possible to highlight differences and similarities among the samples concerning several parameters related to the cerium oxide phase, such as ceria crystalline domain size and local environment, the initial contact between the metal and the oxide, the ceria oxidation state among others. However, a clear identification of a possible main ceria parameter governing the reaction turned out to be challenging and a direct correlation between the properties that were observed by both *ex situ* and *in situ* experiments and the catalyst activity could not be clearly made. The main parameter affecting activity seems to be ceria loading; however, the increase in specific reaction rate values due to the presence of ceria was significantly smaller than predicted by theory considering a Pt–O–Ce interface [27]. These results suggest that the odds to create the true active sites might be the limiting factor in these samples and that they are related to the contact to highly dispersed Ce-O_x species. Nevertheless, how different species of ceria, such as highly dispersed CeO_x species in contact with alumina and few nm-sized crystallites of ceria operate in water activation and intermediates formation has still to be deeper understood.

Acknowledgements

The authors are grateful for the financial support of FAPESP (Fundação de Apoio à Pesquisa do Estado de São Paulo), proc. 2011/50727-9, 2010/52291-0, 2012/00523-0 (BEPE program), and

CNPq (Conselho Nacional de Desenvolvimento Científico e Tecnológico). We thank the Brazilian Synchrotron Light Laboratory (LNLS) for the access to the XAFS1 beamline and XPS facilities and the Brazilian Nanotechnology National Laboratory (LNNano) for the access to the TEM. LNLS staff is acknowledged by the support during synchrotron measurements, in special Dr. D.C. Oliveira for the support during the XPS experiments. Acknowledges to ESRF for granting beamtime, on BM23, in the framework of the scientific collaboration with the University of Campinas and the Federal University of São Carlos during the PhD Thesis of D. M. Meira.

Appendix A. Supplementary data

Supplementary data associated with this article can be found, in the online version, at <http://dx.doi.org/10.1016/j.apcatb.2016.04.025>.

Bibliography

- [1] D.E. Lloyd, *Catalysis Handbook*, Manson Pub., England, 1996.
- [2] K.G. Azzam, I.V. Babich, K. Seshan, L. Lefferts, Bifunctional catalysts for single-stage water–gas shift reaction in fuel cell applications. Part 1. Effect of the support on the reaction sequence, *J. Catal.* 251 (2007) 153–162, <http://dx.doi.org/10.1016/j.jcat.2007.07.010>.
- [3] J.H. Pazmiño, M. Shekhar, W. Damion Williams, M. Cem Akatay, J.T. Miller, W. Nicholas Delgass, et al., Metallic Pt as active sites for the water–gas shift reaction on alkali-promoted supported catalysts, *J. Catal.* 286 (2012) 279–286, <http://dx.doi.org/10.1016/j.jcat.2011.11.017>.
- [4] G. Jacobs, P. Patterson, U. Graham, A. Crawford, A. Dozier, B. Davis, Catalytic links among the water–gas shift, water-assisted formic acid decomposition, and methanol steam reforming reactions over Pt-promoted thoria, *J. Catal.* 235 (2005) 79–91, <http://dx.doi.org/10.1016/j.jcat.2005.07.010>.
- [5] Y. Nagai, T. Hirabayashi, K. Dohmae, N. Takagi, T. Minami, H. Shinjoh, et al., Sintering inhibition mechanism of platinum supported on ceria-based oxide and Pt-oxide-support interaction, *J. Catal.* 242 (2006) 103–109, <http://dx.doi.org/10.1016/j.jcat.2006.06.002>.
- [6] I.D. González, R.M. Navarro, W. Wen, N. Marinkovic, J.A. Rodríguez, F. Rosa, et al., A comparative study of the water gas shift reaction over platinum catalysts supported on CeO₂, TiO₂ and Ce-modified TiO₂, *Catal. Today* 149 (2010) 372–379, <http://dx.doi.org/10.1016/j.cattod.2009.07.100>.
- [7] H. Yao, Ceria in automotive exhaust catalysts I. Oxygen storage, *J. Catal.* 86 (1984) 254–265, [http://dx.doi.org/10.1016/0021-9517\(84\)90371-3](http://dx.doi.org/10.1016/0021-9517(84)90371-3).
- [8] A. Trovarelli, *Catalysis by Ceria and Related Materials*, Imperial College Press, 2002.
- [9] D. Pierre, W. Deng, M. Flytzani-Stephanopoulos, The importance of strongly bound Pt–CeO_x species for the water–gas shift reaction: catalyst activity and stability evaluation, *Top. Catal.* 46 (2007) 363–373, <http://dx.doi.org/10.1007/s11244-007-9013-8>.
- [10] M. Hatanaka, N. Takahashi, T. Tanabe, Y. Nagai, K. Dohmae, Y. Aoki, et al., Ideal Pt loading for a Pt/CeO₂-based catalyst stabilized by a PtO_x bond, *Appl. Catal. B Environ.* 99 (2010) 336–342, <http://dx.doi.org/10.1016/j.apcatb.2010.07.003>.
- [11] K. Nagai, Y. Dohmae, N. Ikeda, T. Takagi, et al., In situ redispersion of platinum autoexhaust catalysts: an on-line approach to increasing catalyst lifetimes? *Angew. Chem. Int. Ed.* 47 (2008) 9303–9306, <http://dx.doi.org/10.1002/anie.200803126>.
- [12] A.P. Ferreira, D. Zanchet, J.C.S. Araújo, J.W.C. Liberatori, E.F. Souza-Aguiar, F.B. Noronha, et al., The effects of CeO₂ on the activity and stability of Pt supported catalysts for methane reforming, as addressed by *in situ* temperature resolved XAFS and TEM analysis, *J. Catal.* 263 (2009) 335–344, <http://dx.doi.org/10.1016/j.jcat.2009.02.026>.
- [13] S. Agarwal, L. Lefferts, B.L. Mojet, Ceria nanocatalysts: shape dependent reactivity and formation of OH, *ChemCatChem* 5 (2013) 479–489, <http://dx.doi.org/10.1002/cctc.201200491>.
- [14] Y. Lykhach, V. Jóhánék, H.A. Aleksandrov, S.M. Kozlov, M. Happel, T. Skála, et al., Water chemistry on model ceria and Pt/cearia catalysts, *J. Phys. Chem. C* 116 (2012) 12103–12113, <http://dx.doi.org/10.1021/jp302229x>.
- [15] J. Vecchietti, A. Bonivardi, W. Xu, D. Stacchiola, J.J. Delgado, M. Calatayud, et al., Understanding the role of oxygen vacancies in the water gas shift reaction on ceria-supported platinum catalysts, *ACS Catal.* 4 (2014) 2088–2096, <http://dx.doi.org/10.1021/cs500323u>.
- [16] L. Barrio, G. Zhou, I.D. Gonzales, M. Estrella, J. Hanson, J.A. Rodriguez, et al., In situ characterization of Pt catalysts supported on ceria modified TiO₂ for the WGS reaction: influence of ceria loading, *Phys. Chem. Chem. Phys.* 14 (2012) 2192–2202, <http://dx.doi.org/10.1039/c1cp22509j>.
- [17] C. Kalamaras, D. Dionysiou, A. Efthathiou, Mechanistic studies of the water–gas shift reaction over Pt/Ce x Zr 1–x O₂ catalysts: the effect of Pt particle size and Zr dopant, *ACS Catal.* 2 (2012) 2729–2742, <http://dx.doi.org/10.1021/cs3006204>.

[18] C.M. Kalamaras, K.C. Petallidou, A.M. Efsthathiou, The effect of La3+-doping of CeO₂ support on the water–gas shift reaction mechanism and kinetics over Pt/Ce1-xLaxO₂-δ, *Appl. Catal. B Environ.* 136–137 (2013) 225–238, <http://dx.doi.org/10.1016/j.apcatb.2013.02.003>.

[19] K.C. Petallidou, A.M. Efsthathiou, Low-temperature water–gas shift on Pt/Ce1-xLaxO₂-δ: effect of Ce/La ratio, *Appl. Catal. B Environ.* 140–141 (2013) 333–347, <http://dx.doi.org/10.1016/j.apcatb.2013.04.007>.

[20] K.C. Petallidou, C.M. Kalamaras, A.M. Efsthathiou, The effect of La3+, Ti4+ and Zr4+ dopants on the mechanism of WGS on ceria-doped supported Pt catalysts, *Catal. Today* 228 (2014) 183–193, <http://dx.doi.org/10.1016/j.cattod.2013.10.081>.

[21] K.C. Petallidou, S. Boghosian, A.M. Efsthathiou, Low-temperature water–gas shift on Pt/Ce0.5La0.5O₂-δ: effect of support synthesis method, *Catal. Today* 242 (2015) 153–167, <http://dx.doi.org/10.1016/j.cattod.2014.06.042>.

[22] C.M. Kalamaras, I.D. Gonzalez, R.M. Navarro, J.L.G. Fierro, A.M. Efsthathiou, Effects of reaction temperature and support composition on the mechanism of water–gas shift reaction over supported-Pt catalysts, *J. Phys. Chem. C* 115 (2011) 11595–11610, <http://dx.doi.org/10.1021/jp201773a>.

[23] C.M. Kalamaras, S. Americanou, A.M. Efsthathiou, Redox vs associative formate with –OH group regeneration WGS reaction mechanism on Pt/CeO₂: effect of platinum particle size, *J. Catal.* 279 (2011) 287–300, <http://dx.doi.org/10.1016/j.jcat.2011.01.024>.

[24] G. Jacobs, B.H. Davis, Surface interfaces in low temperature water–gas shift: the metal oxide synergy, the assistance of co-adsorbed water, and alkali doping, *Int. J. Hydrogen Energy* 35 (2010) 3522–3536, <http://dx.doi.org/10.1016/j.ijhydene.2010.01.055>.

[25] R. Burch, A. Goguet, F.C. Meunier, A critical analysis of the experimental evidence for and against a formate mechanism for high activity water–gas shift catalysts, *Appl. Catal. A Gen.* 409–410 (2011) 3–12, <http://dx.doi.org/10.1016/j.apcata.2011.09.034>.

[26] A.A. Phatak, N. Koryabkina, S. Rai, J.L. Ratts, W. Ruettinger, R.J. Farrauto, G.E. Blau, W.N. Delgass, F.H. Ribeiro, Kinetics of the water–gas shift reaction on Pt catalysts supported on alumina and ceria, *Catal. Today* 123 (2007) 224–234, <http://dx.doi.org/10.1016/j.cattod.2007.02.031>.

[27] S. Aranifard, S.C. Ammal, A. Heyden, On the importance of metal–oxide interface sites for the water–gas shift reaction over Pt/CeO₂ catalysts, *J. Catal.* 309 (2014) 314–324, <http://dx.doi.org/10.1016/j.jcat.2013.10.012>.

[28] S. Aranifard, S.C. Ammal, A. Heyden, On the importance of the associative carboxyl mechanism for the water–gas shift reaction at Pt/CeO₂ interface sites, *J. Phys. Chem. C* 118 (2014) 6314–6323, <http://dx.doi.org/10.1021/jp5000649>.

[29] A. Bruix, J.A. Rodriguez, P.J. Ramírez, S.D. Senanayake, J. Evans, J.B. Park, et al., A new type of strong metal–support interaction and the production of H₂ through the transformation of water on Pt/CeO₂ (111) and Pt/CeO(x)/TiO₂ (110) catalysts, *J. Am. Chem. Soc.* 134 (2012) 8968–8974, <http://dx.doi.org/10.1021/ja302070k>.

[30] J.A. Farmer, C.T. Campbell, Ceria maintains smaller metal catalyst particles by strong metal–support bonding, *Science* 329 (2010) 933–936, <http://dx.doi.org/10.1126/science.1191778>.

[31] M. Cargnello, T.R. Doan-Nguyen, R.E. Gordon, E. a Stach, R.J. Gorte, et al., Control of metal nanocrystal size reveals metal–support interface role for ceria catalysts, *Science* 341 (2013) 771–773, <http://dx.doi.org/10.1126/science.1240148>.

[32] C.M.Y. Yeung, K.M.K. Yu, Q.J. Fu, D. Thompsett, M.I. Petch, S.C. Tsang, Engineering Pt in ceria for a maximum metal–support interaction in catalysis, *J. Am. Chem. Soc.* 127 (2005) 18010–18011, <http://dx.doi.org/10.1021/ja056102c>.

[33] P. Sonström, D. Arndt, X. Wang, V. Zielasek, M. Bäumer, Ligand capping of colloidally synthesized nanoparticles—a way to tune metal–support interactions in heterogeneous gas–phase catalysis, *Angew. Chem. Int. Ed.* 50 (2011) 3888–3891, <http://dx.doi.org/10.1002/anie.201004573>.

[34] W. Xu, R. Si, S.D. Senanayake, J. Llorca, H. Idriss, D. Stacchiola, et al., In situ studies of CeO₂–supported Pt, Ru, and Pt–Ru alloy catalysts for the water–gas shift reaction: active phases and reaction intermediates, *J. Catal.* 291 (2012) 117–126, <http://dx.doi.org/10.1016/j.jcat.2012.04.013>.

[35] J.A. Rodriguez, P. Liu, J. Hrbek, J. Evans, M. Pérez, Water gas shift reaction on Cu and Au nanoparticles supported on CeO₂ (111) and ZnO(0001): intrinsic activity and importance of support interactions, *Angew. Chem. Int. Ed. Engl.* 46 (2007) 1329–1332, <http://dx.doi.org/10.1002/anie.200603931>.

[36] C. Ledesma, J. Yang, D. Chen, A. Holmen, Recent approaches in mechanistic and kinetic studies of catalytic reactions using SSITKA technique, *ACS Catal.* 4 (2014) 4527–4547, <http://dx.doi.org/10.1021/cs501264f>.

[37] A.M. Efsthathiou, in: J. Spivey, K.M. Dooley, Y.-F. Han (Eds.), *Catalysis*, vol. 28, RSC, 2016.

[38] G. Jacobs, P.M. Patterson, U.M. Graham, D.E. Sparks, B.H. Davis, Low temperature water–gas shift: kinetic isotope effect observed for decomposition of surface formates for Pt/ceria catalysts, *Appl. Catal. A: Gen.* 269 (2004) 63–73.

[39] J.P. Clay, J.P. Greeley, F.H. Ribeiro, W.N. Delgass, W.F. Schneider, DFT comparison of intrinsic WGS kinetics over Pd and Pt, *J. Catal.* 320 (2014) 106–117, <http://dx.doi.org/10.1016/j.jcat.2014.09.026>.

[40] G.N. Vayssilov, Y. Lykhach, A. Migani, T. Staudt, G.P. Petrova, N. Tsud, et al., Support nanostructure boosts oxygen transfer to catalytically active platinum nanoparticles, *Nat. Mater.* 10 (2011) 310–315, <http://dx.doi.org/10.1038/nmat2976>.

[41] M. Gonzalez Castaño, T.R. Reina, S. Ivanova, M.A. Centeno, J.A. Odriozol, Pt vs. Au in water–gas shift reaction, *J. Catal.* 314 (2014) 1–9, <http://dx.doi.org/10.1016/j.jcat.2014.03.014>.

[42] F.F. Tao, M. Salmeron, In situ studies of chemistry and structure of materials in reactive environments, *Science* 331 (2011) 171–174, <http://dx.doi.org/10.1126/science.1197461>.

[43] A. Patolla, P. Baumann, W. Xu, S.D. Senanayake, J.A. Rodriguez, A.I. Frenkel, Characterization of metal–oxide catalysts in operando conditions by combining X-ray absorption and raman spectroscopies in the same experiment, *Top. Catal.* 56 (2013) 896–904, <http://dx.doi.org/10.1007/s11244-013-0053-y>.

[44] C.N. Ávila-Neto, J.W.C. Liberatori, A.M. da Silva, D. Zanchet, C.E. Hori, F.B. Noronha, et al., Understanding the stability of Co-supported catalysts during ethanol reforming as addressed by in situ temperature and spatial resolved XAFS analysis, *J. Catal.* 287 (2012) 124–137, <http://dx.doi.org/10.1016/j.jcat.2011.12.013>.

[45] D. Koningsberger, In situ X-ray absorption spectroscopy as a unique tool for obtaining information on hydrogen binding sites and electronic structure of supported Pt catalysts: towards an understanding of the compensation relation in alkane hydrogenolysis, *J. Catal.* 216 (2003) 178–191, [http://dx.doi.org/10.1016/S0021-9517\(02\)00135-5](http://dx.doi.org/10.1016/S0021-9517(02)00135-5).

[46] J.A. Rodriguez, J.C. Hanson, D. Stacchiola, S.D. Senanayake, In situ/operando studies for the production of hydrogen through the water–gas shift on metal oxide catalysts, *Phys. Chem. Chem. Phys.* 15 (2013) 12004–12025, <http://dx.doi.org/10.1039/C3CP50416F>.

[47] S. Bordiga, E. Groppo, G. Agostini, J.A. Van Bokhoven, C. Lamberti, Reactivity of surface species in heterogeneous catalysts probed by In situ X-ray absorption techniques, *Chem. Rev.* 113 (2013) 1736–1850, <http://dx.doi.org/10.1021/cr2000898>.

[48] V.V. Pushkarev, Z. Zhu, K. An, A. Hervier, Gabor A. Somorjai, Monodisperse metal nanoparticle catalysts: synthesis, characterizations, and molecular studies under reaction conditions, *Top. Catal.* 55 (2012) 1257–1275, <http://dx.doi.org/10.1007/s11244-012-9915-y>.

[49] R.U. Ribeiro, D.M. Meira, C.B. Rodela, D.C. Oliveira, J.M.C. Bueno, D. Zanchet, Probing the stability of Pt nanoparticles encapsulated in sol–gel Al₂O₃ using in situ and ex situ characterization techniques, *Appl. Catal. A Gen.* 485 (2014) 108–117, <http://dx.doi.org/10.1016/j.apcata.2014.07.039>.

[50] P.J.S. Prieto, a. P. Ferreira, P.S. Haddad, D. Zanchet, J.M.C. Bueno, Designing Pt nanoparticles supported on CeO₂–Al₂O₃: synthesis, characterization and catalytic properties in the steam reforming and partial oxidation of methane, *J. Catal.* 276 (2010) 351–359, <http://dx.doi.org/10.1016/j.jcat.2010.09.025>.

[51] A.P. Ferreira, D. Zanchet, R. Rinaldi, U. Schuchardt, S. Damyanova, J.M.C. Bueno, Effect of the CeO₂ content on the surface and structural properties of CeO₂–Al₂O₃ mixed oxides prepared by sol–gel method, *Appl. Catal. A Gen.* 388 (2010) 45–56, <http://dx.doi.org/10.1016/j.apcata.2010.08.033>.

[52] L. Wang, F. Meng, Oxygen vacancy and Ce³⁺ ion dependent magnetism of monocrystal CeO₂ nanopoles synthesized by a facile hydrothermal method, *Mater. Res. Bull.* 48 (2013) 3492–3498, <http://dx.doi.org/10.1016/j.materresbull.2013.05.036>.

[53] F. Meng, L. Wang, J. Cui, Controllable synthesis and optical properties of nano-CeO₂ via a facile hydrothermal route, *J. Alloys Compd.* 556 (2013) 102–108, <http://dx.doi.org/10.1016/j.jallcom.2012.12.096>.

[54] D. Wang, Y. Kang, V. Doan-Nguyen, J. Chen, R. Küngas, N.L. Wieder, et al., Synthesis and oxygen storage capacity of two-dimensional ceria nanocrystals, *Angew. Chem. Int. Ed. Engl.* 50 (2011) 4378–4381, <http://dx.doi.org/10.1002/anie.201101043>.

[55] G. Guilera, B. Gorges, S. Pascarelli, H. Vitoux, M.A. Newton, C. Prestipino, et al., Novel high-temperature reactors for in situ studies of three-way catalysts using turbo-XAS, *J. Synchrotron Radiat.* 16 (2009) 628–634, <http://dx.doi.org/10.1107/S0909049509026521>.

[56] J.M. Smith, H.C. Van Ness, M.M. Abbott, *Introduction to Chemical Engineering Thermodynamics*, 7th ed., McGraw-Hill's, USA, 2005.

[57] G.F. Froment, K.B. Bischoff, J. De Wilde, *Chemical Reactor Analysis and Design*, 3rd edition, John Wiley & Sons, Inc., 2011.

[58] R.B. Duarte, S. Damyanova, D.C. de Oliveira, C.M.P. Marques, J.M.C. Bueno, Study of Sm₂O₃–doped CeO₂–Al₂O₃–supported Pt catalysts for partial CH₄ oxidation, *Appl. Catal. A Gen.* 399 (2011) 134–145, <http://dx.doi.org/10.1016/j.apcata.2011.03.045>.

[59] R.B. Duarte, M. Nachtegaal, J.M.C. Bueno, J.A. van Bokhoven, Understanding the effect of Sm₂O₃ and CeO₂ promoters on the structure and activity of Rh/Al₂O₃ catalysts in methane steam reforming, *J. Catal.* 296 (2012) 86–98, <http://dx.doi.org/10.1016/j.jcat.2012.09.007>.

[60] M.J. Kappers, J.H. van der Maas, Correlation between CO frequency and Pt coordination number. A DRIFT study on supported Pt catalysts, *Catal. Letters* 10 (1991) 365–373, <http://dx.doi.org/10.1007/BF00769171>.

[61] M. Scheffler, The influence of lateral interactions on the vibrational spectrum of adsorbed CO, *Surf. Sci.* 81 (1979) 562–570, [http://dx.doi.org/10.1016/0039-6028\(79\)90120-1](http://dx.doi.org/10.1016/0039-6028(79)90120-1).

[62] B.A. Riguette, S. Damyanova, G. Gouliev, C.M.P. Marques, L. Petrov, J.M.C. Bueno, Surface behavior of alumina-supported Pt catalysts modified with cerium as revealed by X-ray diffraction, X-ray photoelectron spectroscopy, and fourier transform infrared spectroscopy of CO adsorption, *J. Phys. Chem. B* 108 (2004) 5349–5358, <http://dx.doi.org/10.1021/jp031167s>.

[63] J. Xu, J.T. Yates, Terrace width effect on adsorbate vibrations: a comparison of Pt(335) and Pt(112) for chemisorption of CO, *Surf. Sci.* 327 (1995) 193–201, [http://dx.doi.org/10.1016/0039-6028\(94\)00849-3](http://dx.doi.org/10.1016/0039-6028(94)00849-3).

[64] H. Song, R. Rioux, J.D. Hoefelmeyer, R. Komor, K. Niesz, M. Grass, et al., Hydrothermal growth of mesoporous SBA-15 silica in the presence of PVP-stabilized Pt nanoparticles: synthesis, characterization, and catalytic properties, *J. Am. Chem. Soc.* 128 (2006) 3027–3037, <http://dx.doi.org/10.1021/ja057383r>.

[65] I. Tankov, K. Arishtirova, J.M.C. Bueno, S. Damyanova, Surface and structural features of Pt/PrO₂–Al₂O₃ catalysts for dry methane reforming, *Appl. Catal. A Gen.* 474 (2013) 135–148, <http://dx.doi.org/10.1016/j.apcata.2013.08.030>.

[66] P. Bazin, O. Saur, J.C. Lavalle, M. Daturi, G. Blanchard, FT-IR study of CO adsorption on Pt/CeO₂: characterisation and structural rearrangement of small Pt particles, *Phys. Chem. Chem. Phys.* 7 (2005) 187–194, <http://dx.doi.org/10.1039/b414159h>.

[67] C. Paun, O.V. Safonova, J. Szlachetko, P.M. Abdala, M. Nachtegaal, J. Sa, et al., Polyhedral CeO₂ nanoparticles: size-dependent geometrical and electronic structure, *J. Phys. Chem. C* 116 (2012) 7312–7317, <http://dx.doi.org/10.1021/jp300342b>.

[68] P.S. Lambrou, C.N. Costa, S.Y. Christou, A.M. Efstatthiou, Dynamics of oxygen storage and release on commercial aged Pd–Rh three-way catalysts and their characterization by transient experiments, *Appl. Catal. B: Environ.* 54 (2004) 237–250, <http://dx.doi.org/10.1016/j.apcatab.2004.06.018>.

[69] H. Cordatos, T. Bunluesin, J. Stubenrauch, J.M. Vohs, R.J. Gorte, Effect of ceria structure on oxygen migration for Rh/ceeria catalysts, *J. Phys. Chem.* 100 (1996) 785–789, <http://dx.doi.org/10.1021/jp952050+>.

[70] H.J. Kalakkad, D.S. Datye, A.K. Robota, Pt–CeO₂ contact and its effect on CO hydrogenation selectivity, *J. Catal.* 148 (1994) 729–736, <http://dx.doi.org/10.1006/jcat.1994.1259>.

[71] S.A. Nunan, J.G. Robota, H.J. Cohn, M.J. Bradley, Physicochemical properties of Ce-containing three-Way catalysts and the effect of Ce on catalyst activity, *J. Catal.* 133 (1992) 309–324, [http://dx.doi.org/10.1016/0021-9517\(92\)90242-A](http://dx.doi.org/10.1016/0021-9517(92)90242-A).

[72] H. Imagawa, A. Suda, K. Yamamura, S. Sun, Monodisperse CeO₂ nanoparticles and their oxygen storage and release properties, *J. Phys. Chem. C* 115 (2011) 1740–1745, <http://dx.doi.org/10.1021/jp109878j>.

[73] G. Jacobs, S. Ricote, U.M. Graham, B.H. Davis, Temperature water–gas shift reaction: interactions of steam and CO with ceria treated with different oxidizing and reducing environments, *Catal. Lett.* 145 (2015) 533–540, <http://dx.doi.org/10.1007/s10562-014-1440-0>.

[74] A. Bruix, A. Migani, G.N. Vayssilov, K.M. Neyman, J. Libuda, F. Illas, Effects of deposited Pt particles on the reducibility of CeO₂ (111), *Phys. Chem. Chem. Phys.* 13 (2011) 11384–11392, <http://dx.doi.org/10.1039/c1cp20950g>.

[75] O.V. Safonova, A.A. Guda, C. Paun, N. Smolentsev, P.M. Abdala, G. Smolentsev, et al., Electronic and geometric structure of Ce³⁺ forming under reducing conditions in shaped ceria nanoparticles promoted by platinum, *J. Phys. Chem. C* 118 (2014) 1974–1982, <http://dx.doi.org/10.1021/jp409571b>.

[76] J.Z. Shyu, W.H. Weber, H.S. Gandhi, Surface characterization of alumina-supported ceria, *J. Phys. Chem.* 92 (1988) 4964–4970, <http://dx.doi.org/10.1021/j100328a029>.

[77] G.N. Vayssilov, A. Migani, K. Neyman, Density functional modeling of the interactions of platinum clusters with CeO₂ nanoparticles of different size, *J. Phys. Chem. C* 115 (2011) 16081–16086, <http://dx.doi.org/10.1021/jp204222k>.

[78] A. Migani, G.N. Vayssilov, S.T. Bromley, F. Illas, K.M. Neyman, Dramatic reduction of the oxygen vacancy formation energy in ceria particles: a possible key to their remarkable reactivity at the nanoscale, *J. Mater. Chem.* 20 (2010) 10535–10546, <http://dx.doi.org/10.1039/c0jm01908a>.

[79] G.N. Migani, S.T. Vayssilov, F. Bromley, Greatly facilitated oxygen vacancy formation in ceria nanocrystallites, *Chem. Commun.* 46 (2010) 5936–5938, <http://dx.doi.org/10.1039/c0cc01091j>.

[80] J. Conesa, Computer modeling of surfaces and defects on cerium dioxide, *Surf. Sci.* 339 (1995) 337–352, [http://dx.doi.org/10.1016/0039-6028\(95\)00595-1](http://dx.doi.org/10.1016/0039-6028(95)00595-1).

[81] D.C. Sayle, S.A. Maicaneanu, G.W. Watson, Nanoparticles, supported on yttrium-stabilized zirconia, *J. Am. Chem. Soc.* 2 (2002) 11429–11439, <http://dx.doi.org/10.1021/ja020657f>.

[82] S. Esch, L. Fabris, T. Zhou, C. Montini, et al., Electron localization determines defect formation on ceria substrates, *Science* 309 (2005) 752–755, <http://dx.doi.org/10.1126/science.1111568>.

[83] D.R. Mullins, P.M. Albrecht, T.-L. Chen, F.C. Calaza, M.D. Biegalski, H.M. Christen, et al., Water dissociation on CeO₂ (100) and CeO₂ (111) thin films, *J. Phys. Chem. C* 116 (2012) 19419–19428, <http://dx.doi.org/10.1021/jp306444h>.

[84] F.C. Meunier, D. Tibiletti, a. Goguet, S. Shekhtman, C. Hardacre, R. Burch, On the complexity of the water–gas shift reaction mechanism over a Pt/CeO₂ catalyst: effect of the temperature on the reactivity of formate surface species studied by operando DRIFT during isotopic transient at chemical steady-state, *Catal. Today* 126 (2007) 143–147, <http://dx.doi.org/10.1016/j.cattod.2006.10.003>.

[85] F.C. Meunier, A. Goguet, C. Hardacre, R. Burch, D. Thompsett, Quantitative DRIFTS investigation of possible reaction mechanisms for the water–gas shift reaction on high-activity Pt- and Au-based catalysts, *J. Catal.* 252 (2007) 18–22, <http://dx.doi.org/10.1016/j.jcat.2007.09.003>.

[86] P. Panagiotopoulou, D.I. Kondarides, Effect of the nature of the support on the catalytic performance of noble metal catalysts for the water–gas shift reaction, *Catal. Today* 112 (2006) 49–52, <http://dx.doi.org/10.1016/j.cattod.2005.11.026>.

[87] T. Bunluesin, R.J. Gorte, G.W. Graham, Studies of the water–gas–shift reaction on ceria-supported Pt, Pd, and Rh: implications for oxygen-storage properties, *Appl. Catal. B: Environ.* 15 (1998) 107–114, [http://dx.doi.org/10.1016/S0926-3373\(97\)00040-4](http://dx.doi.org/10.1016/S0926-3373(97)00040-4).

[88] J. Ke, W. Zhu, Y. Jiang, R. Si, Y.-J. Wang, S.-C. Li, et al., Strong local coordination structure effects on subnanometer PtO_x clusters over CeO₂ nanowires probed by low-temperature CO oxidation, *ACS Catal.* 5 (2015) 5164–5173, <http://dx.doi.org/10.1021/acscatal.5b00832>.

[89] M. Yang, J. Liu, S. Lee, B. Zugic, J. Huang, L.F. Allard, et al., A common single-site Pt(II)-O(OH)x-species stabilized by sodium on active and inert supports catalyzes the water–gas shift reaction, *J. Am. Chem. Soc.* 137 (2015) 3470–3473, <http://dx.doi.org/10.1021/ja513292k>.

[90] M.T. Paffett, S.C. Gebhard, R.G. Windham, B.E. Koel, Chemisorption of CO, H₂, and O₂ on ordered Sn/Pt(111) surface alloys, *Society* 94 (1990) 6831–6839, <http://dx.doi.org/10.1021/j100380a053>.

[91] G. Pirug, H.P. Bonzel, G. Broden, The adsorption of potassium on Pt(111) and its effect on oxygen adsorption, *Surf. Sci.* 122 (1982) 1–20, [http://dx.doi.org/10.1016/0039-6028\(82\)90055-3](http://dx.doi.org/10.1016/0039-6028(82)90055-3).